Available online at www.sciencedirect.com

SCIENCE DIRECT®

PERGAMON

International Journal of Multiphase Flow 29 (2003) 629–653

International Journal of Multiphase Flow

www.elsevier.com/locate/ijmulflow

Instabilities on a free falling jet under an internal flow breakup mode regime

J.B. Blaisot *, S. Adeline

UMR CNRS 6614 – CORIA, Laboratoire de Thermodynamique, Université et INSA de Rouen, 76801 Saint Etienne du Rouvray, France

Received 24 April 2001; received in revised form 26 January 2003

Abstract

Instabilities leading to the breakup of low velocity liquid jets are investigated experimentally. Pulsed shadowgraphy was used to measure local quantities on the wavy shape of the jets with an anamorphic imaging setup. Statistical recording is employed to determine the mean characteristics of the instabilities and time-resolved recording is used to follow individual waves along the jet axis. Particular attention has been paid to the changes that occur in the breakup process at the critical point of the stability curves for jets under internal flow breakup mode regime. For such jets, the critical point is not driven by aerodynamic effects and is not correctly predicted by available theories. It is shown that these jets follow the linear theory of Weber up to the critical point. The growth rate and the wave number increase steeply after the critical point. Evidence is put on the role of the relaxation of the velocity profile in the stability of the jets under internal flow breakup mode regime.

Keywords: Liquid jet breakup; Instability; Anamorphic imaging; Wave measurements

1. Introduction

A liquid jet is naturally unstable and breaks up into droplets. The mode of disintegration is strongly related to the jet character and to the velocity difference $\Delta U = |U_l - U_g|$ between the liquid and the surrounding gas. This difference controls the level of the aerodynamic forces. For the case of a low liquid velocity jet in an ambient gas at rest, the aerodynamic forces are negligible and the jet

* Corresponding author.
E-mail address: blaisot@coria.fr (J.B. Blaisot).
URL: http://www.coria.fr.

0301-9322/03/$ - see front matter
doi:10.1016/S0301-9322(03)00020-X

breaks up into drops with a diameter comparable to the jet diameter under the capillary pinching phenomenon. This is the Rayleigh mode regime. For high values of ΔU (high liquid or gas velocity), the instabilities lead the jet to break up into drops with diameters much smaller than the jet diameter. This latter case corresponds to the Taylor mode or atomization regime (Lin and Lian, 1990).

The breakup of the jet can additionally be dependent on the nozzle geometry. Karasawa et al. (1992) clearly showed the effect of the nozzle length on the development of instabilities on the liquid jet surface. When the nozzle length increases, the jet surface shape changes from smooth to corrugated. The initial velocity profile at the nozzle exit can thus have a real influence on the liquid jet stability and the sensitivity of the jet to the velocity profile is particularly true for low mean velocity (laminar) flows.

In most experiments on free falling liquid jets, the disintegration process is characterised through the stability curve (see Fig. 1). This curve represents the breakup length L_{bu} versus the liquid jet velocity U_{l} where the breakup length is the height of the continuous column of liquid at the nozzle exit. This length increases with U_{l} until it reaches a maximum, the critical point (point C in Fig. 1). This point marks the end of the Rayleigh regime. Beyond the critical point, the jet is under what is classically called the first wind induced regime. For jets not depending on the nozzle geometry, the decrease of the breakup length beyond point C is actually related to the increasing influence of aerodynamic forces. The mechanism of breakup changes progressively from axisymmetrical capillary pinching (varicose breakup) to asymmetrical sinuous breakup and then to wind loading. For jets for which the critical point changes with the nozzle geometry, the change of mechanism cannot be associated to an increase of aerodynamic forces. Indeed, Leroux et al. (1997) and Iciek (1982) showed that in this case long nozzle lengths induce small critical velocities. For the longest tubes, the critical velocity is reached for flow conditions where the aerodynamic forces can be neglected. Moreover, Leroux et al. (1997) found that these jets are characterised by a critical velocity independent of the surrounding ambient gas pressure, which confirms the weak influence of aerody-

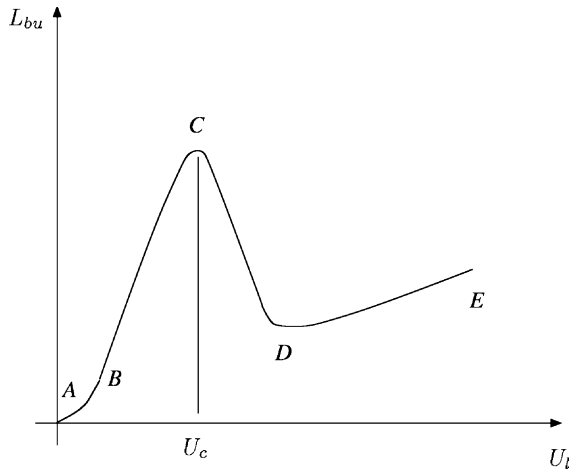

Fig. 1. *Stability curve.* Jet breakup length L_{bu} as a function of the jet velocity U_{l}. The linear increase of L_{bu} (BC) corresponds to the Rayleigh regime of instability. The first maximum at point C, the critical point, marks the transition between the Rayleigh regime and the ABM regime or the IFBM regime. The regimes for very low velocities (dripping regime AB) or very high velocities (second wind induced DE) are not explored in the present work.

namic effects. Leroux et al. (1996) classified three types of behaviour of the critical point of jets in different ambient conditions. Jets of the first type are characterised by a critical velocity that is independent of the surrounding ambient gas pressure. For these jets, the critical point is controlled by the liquid flow only (liquid properties, flow regime, velocity profile,...). We refer to the regime occurring beyond the critical point of jets of the first type as an *internal flow breakup mode* (IFBM) regime. For jets of the third type, the critical point is related to the effect of the aerodynamic forces. The regime beyond point C could be designated in this case by *aerodynamic breakup mode* (ABM) regime or *"truly" first wind-induced* regime. The jets of the second type have an intermediate behaviour between jets of type one and three. The present work is focused on the transition between Rayleigh and IFBM regimes for laminar jets under the action of axisymmetrical disturbances.

Linear theories developed more than a century ago, are able to predict the disintegration of liquid jets under the action of Rayleigh or Taylor instabilities (McCarthy and Molloy, 1974; Bogy, 1979; Eggers, 1997; Lin and Reitz, 1998), but despite the abundant literature on this subject, there is as yet no quantitative treatment of the nozzle geometry effect. The critical velocities of IFBM regime jets are far below the value predicted by the theory. Sterling and Sleicher (1975) suggested that the origin of the critical point has to be found in the relaxation of the velocity profile along the jet axis. Leib and Goldstein (1986a) and Ibrahim and Marshall (2000) have shown a great dependence of the growth rate of the instability on the velocity profile but do not include the relaxation of the velocity profile along the jet axis in their analyses. Penchev and Radev (1977) and Radev et al. (1983) showed a variation of the growth rate and of the wave number along the jet in a numerical analyses on the stability of a jet in a liquid–liquid system. The change of the critical velocity for IFBM regime jets could then be related to a change in the growth rate of perturbation due to the effect of the velocity profile rearrangement as proposed by Sterling and Sleicher. Phinney (1972) suggested that the critical point is in fact related to an increase of the initial amplitude of perturbation at the nozzle exit and not to a modification of the growth rate. Unfortunately, experimental results on free falling jets found in the literature are concerned with breakup length measurements only. No data are reported on initial amplitude or growth rate of perturbation for these jets, so the question of the origin of the critical point has not yet been solved.

A measurement technique has been developed by Blaisot and Adeline (2000) to access to these quantities. The technique is based on an anamorphic imaging configuration combined here with time-resolved as well as statistical measurements. Growth rates and initial disturbance levels as well as wave numbers and phase velocities are determined for liquid jets emanating from nozzles of different length to diameter ratios. It is clearly shown that the occurrence of the critical point is related to a change of the growth rate and that this change is different from what happens for ABM regime jets. The experimental setup is presented in Section 2. The measurement results follow and a conclusion ends the paper.

2. Experimental setup

2.1. Jet injection

Water is used for the liquid. Four nozzles of internal radius $a = 300$ μm and different length L are used ($L/2a = 10$, 27, 125, 200). The nozzle lengths were chosen in order to cover different

initial exit conditions from uniform ($L/2a = 10$) to fully developed laminar velocity profile ($L/2a = 200$). The nozzles are connected to a small tranquillization chamber and a convergent to ensure a flat velocity profile condition at the nozzle entrance. The water is injected from a pressurised cylindrical tank. Mass-averaged mean flow velocity U_l was changed from 0.8 to 6.6 m/s by changing of the tank pressure.

2.2. Velocity profile at the nozzle exit

The small size of the nozzle diameter prevents the use of any experimental technique to measure the velocity profile $U(r)$ at the nozzle exit. The velocity profiles are therefore computed with the commercial CFD software FLUENT for each nozzle. It has been verified that the velocity profile at the nozzle entrance is always flat whatever the nozzle length and the injection pressure. The profiles at the nozzle exit are fitted with the following expression:

$$U_e(r,\beta) = U_0 \frac{\tanh[\beta(1-(r/a)^2)]}{\tanh(\beta)} \tag{1}$$

where U_0 is the velocity on the axis ($r = 0$) and β is a non-dimensional parameter. The expression of Eq. (1) is the analytic form that was found to be the closest to the computed profiles. The profiles range from the flat profile for $\beta \to \infty$ to the parabolic profile for $\beta = 0$. The range of values for β has been reduced to [0.1–100] without any loss of accuracy. For $\beta = 0.1$ the profile is already parabolic (the difference between $U_e(r, 0.1)$ and $U_0(1-(r/a)^2)$ is lower than 0.2% for every value of r). For $\beta = 100$, $U_e(r, 100) = 1$ up to $r/a = 0.98$. The results for β versus U_l are shown in Fig. 2. The profile remains parabolic for the two longest nozzles ($\beta < 0.5$). We suppose that the profile relaxation effect will be noticeable for these nozzles. Only the profiles for $L/2a = 10$ and 27 really differ from the parabolic profile and become flatter as U_l increases. For $L/2a = 10$ and $U_l = 5.0$ m/s the profile presents a plateau at the centre line over half the jet diameter (profile for $\beta = 2.4$ on Fig. 2). The low values of β show that it is difficult to produce a low velocity jet with a flat velocity profile at the nozzle exit. However, the range of velocity profiles obtained with the four tested nozzles is sufficiently wide to generate the different desired stability behaviours.

2.3. Jet imaging

Pulsed shadowgraphy is used to measure the local properties of the jet interface shape. A white incoherent stroboscope source (EG&G MVS 2600) with a spark duration of about 10 μs is used in a back-lighting configuration. This duration is short enough to effectively freeze the jet movement and prevent blur effects on the images. The light source is collimated by a condenser in such a way that the illumination of the jet is weakly divergent. The anamorphic imaging system presented in Fig. 3 is similar to the one used by Collicott et al. (1994). It is composed of a set of two cylindrical lenses. The magnification is 0.17 in the stream-wise (vertical) direction z and 5.9 in the radial direction r giving a magnification ratio of about 38:1. Images are recorded either with a drum (film) camera or with a CCD camera. The visualisation area in the jet plane is around 60 mm long

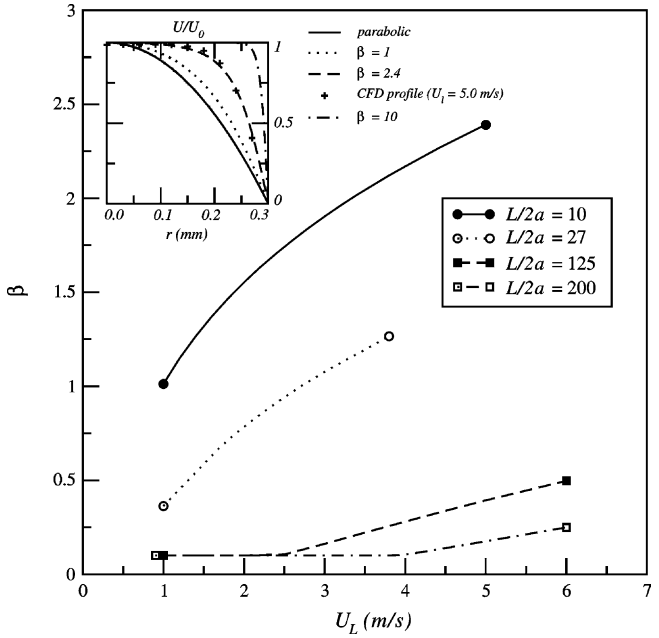

Fig. 2. *Velocity profile at the nozzle exit.* Evolution of the parameter β with U_l for each nozzle. Velocity profiles remain parabolic for the two longest nozzles whereas they reach the flat shape for the two shortest nozzles when U_l increases. Profile shapes $U_e(r,\beta)$ are also plotted for $\beta = 0$ (parabolic), 1, 2.4 and 10 in the upper left hand corner. The points obtained from CFD results for $U_l = 5.0$ m/s and $L/2a = 10$ are also reported with the profile shapes.

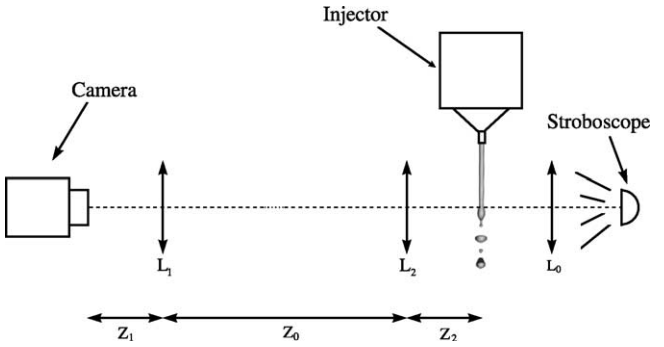

Fig. 3. *Imaging setup.* Pulsed shadowgraphy is performed with an anamorphic configuration. The axes of the cylindrical lenses L_1 and L_2 are perpendicular to each other and the lengths Z_0, Z_1 and Z_2 are such that the magnification ratio is 38:1. L_0 is a collimator lens.

and 1 mm wide. As the jet is backlight illuminated, it appears as black over white. Images of the jet obtained with each recording system are presented in Figs. 4 and 5.

It is important to note that the anamorphic imaging system is very sensitive to angles. If the vertical axes of the jet and the optical setup are not rigorously parallel, the angle between the axes is strongly amplified in the image. Therefore, due to the slight change of the verticality of the jet

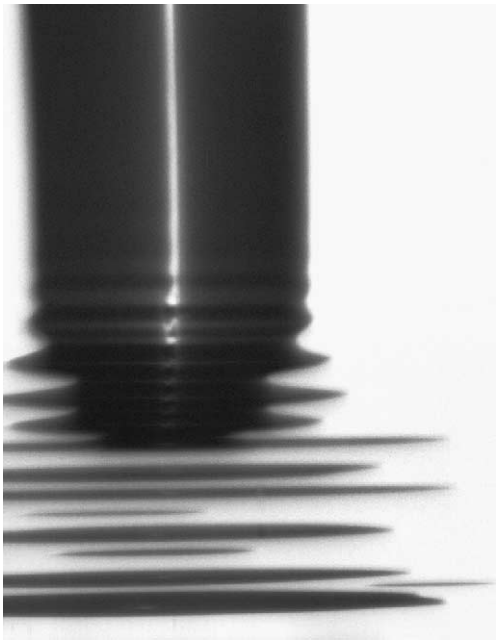

Fig. 4. *Statistical technique image.* Images are recorded with a CCD camera at the video framing rate of 25 images/s. The jet width is dilated by the anamorphic imaging setup. Droplets appear as flat disks but are really spherical ($L/2a = 200$, $U_l = 1.60$ m/s).

from one experiment to the other, it was difficult to adjust the optical setup in such a way that the image of the jet remains parallel to the side of the camera. The orientation of the jet in Fig. 5 is a consequence of a weak angle between the jet and the vertical optical axis but, as the jet orientation remains the same during any one experiment (U_l fixed), is not due to a lateral swing of the jet.

The penultimate waves in Figs. 4 and 5 present a smaller amplitude than the neighbouring waves. It will be shown with the time-resolved technique that this corresponds in fact to a wave (the next to last) which was triggered with a smaller initial amplitude than the preceding and following ones, leading to a less amplified wave downstream in the jet. Each individual wave tracked during its movement actually grows monotonously along the jet axis.

2.4. Image recording

Two different recording systems have been used, each one being devoted to a particular analysis. Time-resolved measurements have been obtained with a Cordin 447/351 rotating drum camera at a framing rate of 1000 images/s. This framing rate corresponds to the maximum repetition rate of the stroboscope. The image resolutions are 14.3 pixels/mm in the stream-wise direction and 609.1 pixels/mm in the radial direction. The low energy per flash of the stroboscope at its maximum repetition rate leads us to use highly sensitive but very granular film (Kodak TMAX ISO 3200). The images, therefore, are of relatively poor quality, as can be seen in Fig. 5, and this quality was not sufficient to allow an automatic numerical treatment of the images.

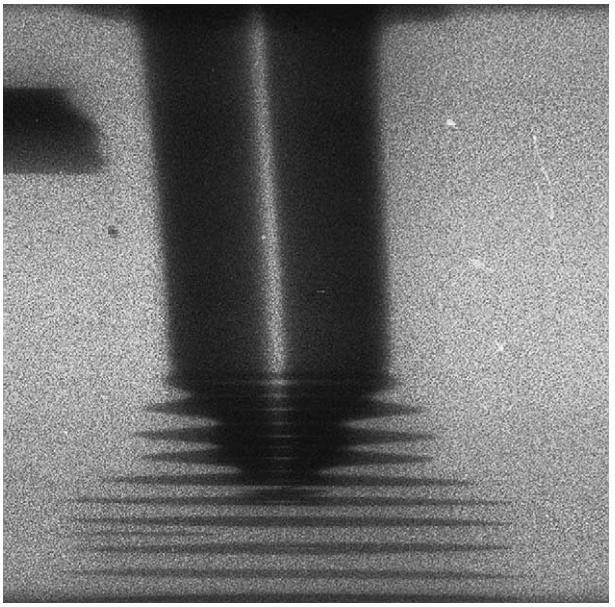

Fig. 5. *Time-resolved technique image.* Images are recorded with a drum camera at a framing rate of 1000 images/s. The poor quality of the image is caused by the granularity of the highly sensitive film used to compensate for the low flash energy of the stroboscope at the highest rate ($L/2a = 27$, $U_l = 1.70$ m/s).

A Sony XC77CE CCD camera was used for the statistical analysis. Images are grabbed on a PC at the video framing rate (25 images/s). A series of 100 images was recorded for each injection condition. Statistical data are obtained by numerical image processing.

2.5. Theoretical background

The radial position of the perturbed jet surface is $r = a + \eta$ where

$$\eta(z,t) = \eta_0 e^{j(kz-\omega t)} \tag{2}$$

for normal modes of perturbation and η_0 is the initial amplitude of the disturbance. In the frame of the temporal analysis, k is real and ω is purely imaginary. The perturbation grows in time only and oscillates along a jet of infinite length. For the spatio-temporal analysis, a semi-infinite jet is considered ($z = 0$ at the nozzle exit) and $k_i = \mathrm{Im}(k)$ and $\omega_r = \mathrm{Re}(\omega)$ are different from zero. Keller et al. (1973) showed that temporal and spatio-temporal analyses converge for $We = (2a\rho_l U_l^2)/\sigma \gtrsim 3.2$. Leib and Goldstein (1986b) showed that the transition from convective ($k_i \neq 0$ and $\omega_i = 0$) to absolute ($k_i \neq 0$ and $\omega_i \neq 0$) instabilities occurs for very low Weber numbers. In practice, absolute instability corresponds to the dripping flow regime, not studied in the present work, so, as the Keller criterion applies, either the temporal or the spatio-temporal analyses can be used to characterise the jet stability.

To compare the theory to naturally perturbed liquid jets it is assumed that the perturbation leading to the breakup of the jet is the one corresponding to the fastest destabilization mode, i.e. the one with the greatest or optimum growth rate ($\omega_i = \omega_{i,opt}$ or $|k_i| = |k_{i,opt}|$). In the frame of the

temporal analysis, the breakup time t_{bu}, i.e. the time needed for the perturbation to reach a magnitude equal to the jet radius, is given by

$$t_{bu} = \frac{1}{\omega_{i,opt}} \ln \frac{a}{\eta_0} \tag{3}$$

and the breakup length L_{bu} is then derived from Eq. (3) using the Galilean transformation $z = z + U_l t$

$$L_{bu} = \frac{U_l}{\omega_{i,opt}} \ln \frac{a}{\eta_0} \tag{4}$$

The breakup length can also be directly obtained from the spatio-temporal analysis

$$L_{bu} = \frac{1}{|k_{i,opt}|} \ln \frac{a}{\eta_0} \tag{5}$$

In most experimental works, breakup lengths are compared to the temporal analysis through Eq. (4) or more rarely to the spatio-temporal analysis through Eq. (5). A constant value is assumed for $\ln a/\eta_0$ for L_{bu} to be compared to the variation of $U_l/\omega_{i,opt}$ or to the variation of $1/|k_{i,opt}|$. In the present experiment, growth rates are measured from the wavy shape of the jet interface, so $\omega_{i,opt}$ and $|k_{i,opt}|$ are directly compared to our measurement without any assumption on the value of $\ln a/\eta_0$. Moreover, $\ln a/\eta_0$ can be evaluated as will be shown below.

Results are compared to the temporal analysis of Rayleigh (1878) and Weber (1931). The equation used for the Weber theory is in fact the one developed by Sterling and Sleicher (Eq. (20) in Sterling and Sleicher, 1975). This equation, derived in the frame of the temporal analysis, is equivalent to the one obtained by Lin and Lian (1990) for the case of the spatio-temporal theory. The last two theories delineate both the Rayleigh and the Taylor modes of instability but include neither the effect of the nozzle geometry nor the velocity profile relaxation. They are, however, the most advanced theories of the linear approach, particularly for the prediction of the critical point. No attempt has been made to use a non-linear theory, since the main interest of non-linear theories is the prediction of satellite droplets, which are not studied in the present work.

2.6. Time-resolved technique

2.6.1. Wave amplitude

The poor image quality obtained with the drum camera prevents the use of computer based image analysis of the jet interface. The amplitude and position of all waves visible to the naked eye are therefore measured manually. The downstream position of a wave, z_m, is defined by the swell location. The amplitude of the perturbation waves, η_m, is defined by half the difference between successive neck and swell radial positions (r_n and r_s, respectively) of a wave as proposed by Goedde and Yuen (1970)

$$\eta_m = (r_s - r_n)/2 \tag{6}$$

Lin and Lian (1990) mentioned that this definition is not consistent with Eq. (2) because η is a local parameter, whereas the definition in Eq. (6) covers half a wavelength. Nevertheless, growth rate values are small enough to allow the application of the slow variation hypothesis: the

amplitude difference between two successive swells is negligible compared to the wavelength. The error induced by the use of Eq. (6) is indeed less than the error produced by $(r_s - r_a)$ since r_a, the local undisturbed radial position at the same downstream position, cannot be easily defined.

2.6.2. Time and spatial diagrams

The amplitude $\eta_m(t)$ and the position $z_m(t)$ of the capillary waves are measured for $t = 0$, $\delta t, 2\delta t, \ldots$ where δt is the time interval between two successive images ($\delta t = 1$ ms in the time-resolved analysis). The time series $\eta_m(t)$ and $z_m(t)$ are analysed through three different types of diagram: $z_m = f(t)$ (Fig. 6a), $\ln(\eta_m/a) = f(t)$ (Fig. 6b) and $\ln(\eta_m/a) = f(z_m)$ (Fig. 6c). In these

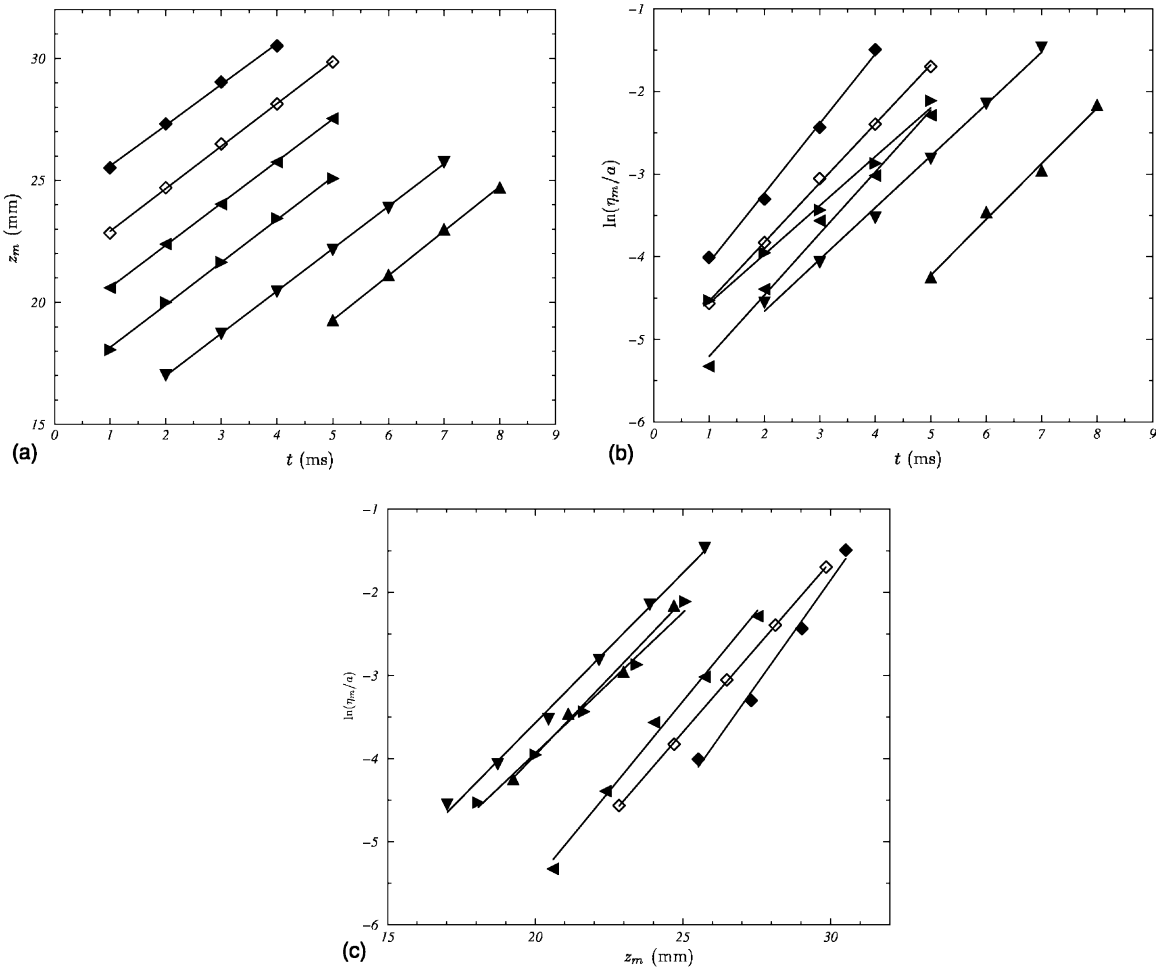

Fig. 6. *Time-resolved diagrams.* (a) Phase velocity is determined from diagram $z_m = f(t)$. The case $L/2a = 27$ and $U_l = 1.70$ m/s gives $c = 1.75$ m/s. (b) The linear increase of the logarithm of the wave amplitude versus time is verified from diagram $\ln(\eta_m/a) = f(t)$. The different slopes result from the variations of growth rates from wave to wave. (c) The spatial increase of the perturbations is obtained from the diagram $\ln(\eta_m/a) = f(z_m)$. The linear increase of $\ln(\eta/a)$ is verified. Perturbation waves are marked by their order of appearance on the jet ◆, first wave; ◇, 2nd; ◄, 3rd; ►, 4th; ▼, 5th; ▲, 6th.

diagrams, each symbol corresponds to a particular wave. The diagram $z_m = f(t)$ is used to measure the phase velocity c, i.e. the velocity of the perturbation, convected along the jet. The two diagrams $\ln(\eta_m/a) = f(t)$ and $\ln(\eta_m/a) = f(z_m)$ represent the temporal and the spatial evolution of the disturbance level, respectively. The linear increase of $\ln(\eta_m/a)$ with time and space is controlled on these diagrams and confirms the "linearity" of the breakup of the Newtonian liquid jets also mentioned by Yarin (1993). The linear increase of $\ln(\eta_m/a)$ has also been reported by Goedde and Yuen (1970) for results on excited liquid jets. They remarked that, even though the neck grows much faster than the swell, the logarithm of the difference between swell and neck grows linearly. Goedde and Yuen did not use a time-resolved technique in their experiment as the jets they study were controlled by an excitation device. In the present case, time-resolved measurements are essential to access to the linear increase of $\ln(\eta_m/a)$ due to the dispersion from wave to wave occurring in free falling jets.

2.6.3. Local wave analysis

The particularity of free falling jets is that, unlike excited jets presenting a regularly increasing shape, they appear to be controlled by a random process. The straight lines in Fig. 6c, each corresponding to a particular wave, are quasi-parallel but not superimposed. The perturbations grow at the same rate, but do not reach the same state, i.e. the same amplitude, at a given downstream position in the jet. The consequence is that the shape of the jet at a given time can show a non-regular increase of the wave amplitude as can be observed in Figs. 4 and 5.

Let us consider individually the perturbations at the jet interface. Each perturbation or single wave is a one wavelength portion of a sinusoid centred on a swell. The displacement of the jet interface for a single wave followed in time is given by

$$\eta_{sw}(z,t) = \eta_{sw_0}\cos(k_r z - \omega_r(t - t_{sw_0}))e^{\omega_i(t-t_{sw_0})} \tag{7}$$

$$k_r z_{sw} - \omega_r(t - t_{sw_0}) = 0 \tag{8}$$

$$-\pi \leqslant k_r(z - z_{sw}) \leqslant \pi \tag{9}$$

where the position of the wave crest is z_{sw} and the initial time t_{sw_0} is such that $t = t_{sw_0}$ when the single wave is at the jet exit ($z_{sw} = 0$). In a first approximation, we consider identical wave number k_r, pulsation ω_r and growth rate ω_i for all the waves, but each single wave has its own initial amplitude η_{sw_0}. This means that the parameters governing the growth conditions are the same for all single waves, but that the chaotic behaviour of the perturbation process leads to different initial conditions. The single wave swell amplitude is then derived from Eqs. (7) and (8):

$$\eta_{sw}(z_{sw}) = \eta_{sw_0} e^{\omega_i \frac{k_r}{\omega_r} z_{sw}} \tag{10}$$

in which η_{sw_0} is the only varying parameter. The variation of η_{sw_0} leads to diagrams $\ln(\eta_{sw}/a)$ versus z_{sw} in which waves are represented by parallel straight lines as in Fig. 6c. The higher η_{sw_0}, the higher the straight line in the diagram. The measured wave amplitude and position η_m and z_m, can be related to the local wave model

$$\eta_m(z_m) = \eta_{sw_0} e^{\omega_i \frac{k_r}{\omega_r} z_m} \tag{11}$$

$$\eta_m(t) = \eta_{sw}(z_{sw}, t) = \eta_{sw_0} e^{\omega_i(t-t_{sw_0})} \tag{12}$$

$$z_m(t) = z_{sw}(t) = \frac{\omega_r}{k_r}(t - t_{sw_0}) \tag{13}$$

Eq. (13) is used to determine the phase velocity $c \equiv \omega_r/k_r$. The relation between temporal and spatial growth rates is derived from Eq. (11)

$$k_i = \omega_i \frac{k_r}{\omega_r} = \frac{\omega_i}{c} \tag{14}$$

and corresponds to Gaster's relation

$$\tilde{k}_i = \tilde{\omega}_i$$

where $\tilde{k}_i = ak_i$ and $\tilde{\omega}_i = (a\omega_i)/c$ are non-dimensional values.

2.7. Statistical technique

The imaging setup used in this section is the same as for the time-resolved technique except for the image recording which is achieved with a CCD camera at a framing rate of 25 images/s. Computer based image analysis is performed. The procedure has been fully presented in a previous paper (Blaisot and Adeline (2000)). A brief remainder of the method is given here.

2.7.1. Image analysis and contour tracing

As shown previously, the jet appears as black over white and, since the background image is not uniform, a ratio of each image to the mean background image is calculated as a first operation. The background image is taken from 30 images without a jet, recorded at the beginning of each experiment. Normalised images present good quality with high contrast and an almost uniform intensity distribution in the region outside the jet. A sub-pixel contour tracing technique is applied to determine the radial position of the liquid–gas interface $r(z)$. The jet is scanned in the radial direction r and the sub-pixel position of the local jet radius is determined from a linear regression of the light profile near the half height grey level.

2.7.2. Wavelet analysis and shape recognition

The jet interface displacement, defined by $\eta(z) = r(z) - a$, is analysed by continuous wavelet transform. The wavelet transform is used for its ability to determine both the position and the size of the waves. The wavelet transform is defined by the inner product

$$W(e,l) = \int_{-\infty}^{+\infty} \eta(z) \frac{1}{\sqrt{e}}, \overline{\psi}\left(\frac{z-l}{e}\right) \mathrm{d}z \tag{15}$$

where the mother wavelet $\psi(z)$ is translated by vector l and scaled by a coefficient e. The wavelet $\psi(z)$ selected in the present study is the Mexican hat function:

$$\psi(z) = \frac{2\pi^{-1/4}}{\sqrt{3}}(1 - z^2)\exp\left(-\frac{z^2}{2}\right) \tag{16}$$

This wavelet is useful to detect wave swells in a signal. The wavelet coefficient $W(e,l)$ is maximum at the position l^* and the scale e^* corresponding to a wave crest in $\eta(z)$. A peak extraction algorithm based on a neighbourhood analysis is applied to $W(e,l)$ to locate local maximum wavelet

coefficients in the (e, l) plane. The peak locations (e^*, l^*), taken as input parameters for a shape recognition method, give indications on local wave positions and spans. For each peak position l^*, the portion of the jet analysed by the shape recognition technique covers a wavelength

$$l^* - 2e^* \leqslant z \leqslant l^* + 2e^* \tag{17}$$

Sine and circular shapes are tested and the best fitting one is automatically chosen. Two shape parameters are determined from the shape recognition: the curvature parameter τ^* which corresponds to the wavelength of the sine shape or the diameter of the circular shape, and the magnitude parameter η^* which corresponds to the magnitude of the sine shape or the radius of the circular shape. For the sine shape, η^* is similar to η_m used for time-resolved measurements. The smallest liquid interface amplitude measurable with this technique is around 3 μm.

The sine shape is detected along the jet axis and the circular shape is validated for the last crest in the contour which corresponds to a drop that is about to detach from the jet. The wave number k_r, the spatial growth rate k_i and the initial disturbance level η_0 are derived from the measurement of l^* and η^* on sine shapes only.

3. Results

3.1. Breakup length

The breakup length L_{bu} is determined with the statistical technique from the extremity of the jet contour. Mean breakup lengths are determined from one hundred points for each jet velocity. The stability curves for the four nozzles are reported in Fig. 7. The prediction of the Weber's theory is also reported in this figure. A constant value for η_0 ($\ln \eta_0/a = -12.4$) has been chosen in such a way that the slope of the theoretical curve fits the experimental points in the Rayleigh regime. As mentioned above, the theory overestimates the critical velocity of the jets under consideration. The experimental critical velocity U_c is determined at the maximum of the stability curve, fitted by a polynomial function. Results are reported in Table 1. The critical velocity and the breakup length at critical point decrease when the nozzle length increases. The consequence is that the range of velocity corresponding to the Rayleigh regime ($U_l < U_c$) is narrower for the longest nozzles.

The breakup lengths of jets in the Rayleigh regime are identical, i.e. the points are well superimposed in the linear part of the stability curves. However, the initial injection conditions for these jets are different. The velocity profiles at the nozzle exit, for example, are not the same. It can be concluded that jets in the Rayleigh regime are not sensitive to the initial injection conditions (McCarthy and Molloy, 1974). As for the critical point, it changes with the nozzle length, so it strongly depends on the initial injection conditions. When the regime changes from Rayleigh to IFBM, the jets become sensitive to the initial injection conditions.

3.2. Phase velocity

The phase velocity $c = \omega_r/k_r$ is derived from Eq. (13):

$$c = \frac{z_m}{(t - t_{sw_0})} \tag{18}$$

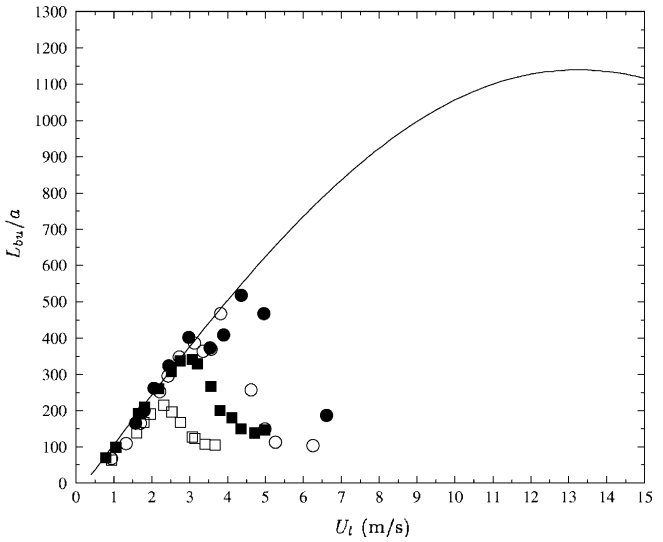

Fig. 7. *Breakup length.* (●), $L/2a = 10$; (○), 27; (■), 125; (□), 200. Critical velocities range from 2.2 m/s ($L/2a = 200$) to 4.4 m/s ($L/2a = 10$). The continuous line is for the Weber theory which overestimates the critical velocity ($U_{c,We} = 13.2$ m/s).

Table 1
Characteristics of the jets at the critical point

	$L/2a$			
	10	27	125	200
U_c (m/s)	4.4	3.8	3.1	2.2
L_{bu}/a	520	470	340	215

The critical velocity U_c and the breakup length L_{bu} at the critical point decrease with the nozzle length L.

The phase velocity of the perturbations is measured from the mean slope of the straight lines in the diagram $z_m = f(t)$ (Fig. 6a). Phase velocities have been measured for the nozzles of length $L/2a = 10$, 27 and 200. For a given nozzle and a fixed mean jet velocity U_l, the values of c present very few dispersions from wave to wave. The results for c versus U_l are reported in Fig. 8. The phase velocity is greater than U_l in every condition and the difference between c and U_l increases with U_l. Actually, c is measured at the extremity of the jet whereas U_l is relevant to the nozzle exit. Effectively, U_l is determined from the mean flow rate of the liquid and the nozzle diameter and not from the jet diameter which decreases along the z axis. The decrease of the diameter is directly related to the jet acceleration due to the combined effects of gravity and profile relaxation.

The effect of profile relaxation on jet acceleration has been analysed by Harmon (1955) who showed that the relaxation from the parabolic profile leads to a limit downstream jet velocity equal to 4/3 times the mass average velocity U_l. The phase velocity reaches the 4/3 limit for $L/2a = 200$ rapidly which confirms the hypothesis of a strong effect of profile relaxation for this nozzle. The same approach as Harmon's is used to compare the computed exit velocity profiles

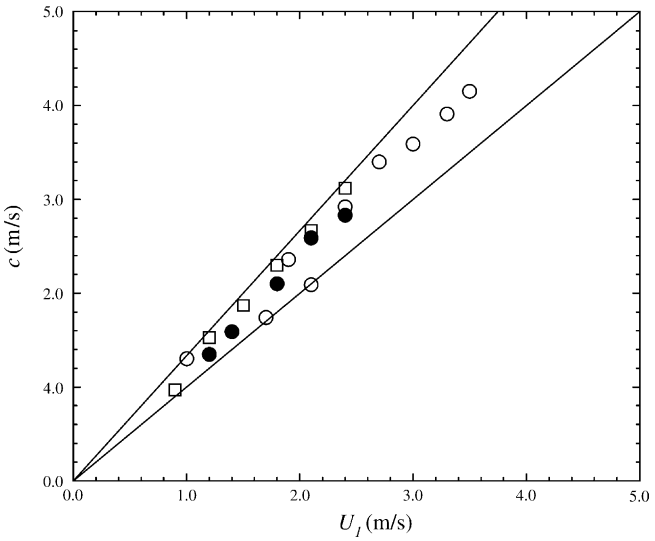

Fig. 8. *Phase velocity.* (●), $L/2a = 10$; (○), 27; (□), 200. Continuous and dashed lines are respectively for $c = U_l$ and $c = 4/3U_l$. The upper limit corresponding to velocity relaxation from a parabolic profile is rapidly reached for $L/2a = 200$.

and the phase velocity measured on the jets. It consists in writing the mass and momentum balance on the jet

$$U_l a^2 = U_f a_f^2 \tag{19}$$

$$\text{and} \quad \dot{M}_0 = \int_0^a \rho_l U_e(r,\beta)^2 2\pi r \, dr = \dot{M}_f = \rho_l U_f^2 \pi a_f^2 \tag{20}$$

The under-script 'f' indicates the final values at the extremity of the jet. By putting Eq. (19) in the expression of the final momentum rate $\dot{M}_f$ we obtain

$$\dot{M}_f = \rho_l U_l c \pi a^2$$

where it is supposed that the downstream jet velocity U_f equals the phase velocity c. The computed initial momentum rate $\dot{M}_0$ and the measured final momentum rate $\dot{M}_f$ are compared in Fig. 9. Indeed, the momentum increases with U_l. The dependence of the initial momentum rate $\dot{M}_0$ on the initial velocity profile is clear. It increases up to 20% between $L/2a = 10$ and 200 at $U_l = 2.8$ m/s, i.e. for β decreasing from 2 to 0.1. The increase of the momentum rate when the velocity profile becomes parabolic is confirmed with the final momentum rate that shows the same trends. Moreover, experimental points and theoretical curves are well superimposed. The velocity profile computations are thus validated by the good agreement found between $\dot{M}_0$ and $\dot{M}_f$.

3.3. Growth rate

The estimation of the wave crest amplitudes on the image given by the time-resolved technique is liable to errors induced by the appreciation of the operator and by the granularity of the images.

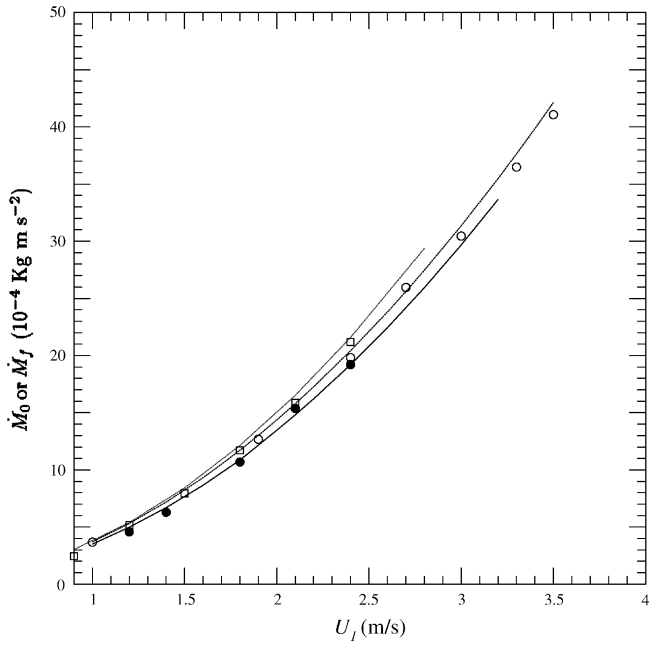

Fig. 9. *Momentum rates.* The initial momentum rate $\dot{M}_0$ is derived from CFD computations of the velocity profile at the nozzle exit (—, $L/2a = 10$; - - -, $L/2a = 27$; ···, $L/2a = 200$). The final momentum rate $\dot{M}_f$ is deduced from phase velocity measurement ((●), $L/2a = 10$; (○), 27; (□), 200). Velocity profile computations are validated by the good agreement between $\dot{M}_0$ and $\dot{M}_f$.

The measurements of ω_i and k_i are thus subject to some discrepancies. Moreover, with this technique, it takes a long time to obtain the required number of measurements, so the statistical technique has been preferred for the measurement of the growth rates.

Growth rates are measured from the diagram $(\ln(\eta^*/a))(l^*)$. Images recorded in the statistical analysis are not related in time so η^* and l^* can be considered as random variables, i.e. the points $(l^*, \ln(\eta^*/a))$ cannot be joined together for a given perturbation. The chaotic behaviour of the perturbation process already mentioned in the local wave analysis paragraph generates scattered diagrams as shown in Fig. 10. This scattering can be simulated from the diagram of the time-resolved technique if the points for each wave in Fig. 6c are not joined together: a scattered set of points similar to the one in Fig. 10 is thus obtained. In fact, the points $(l^*, \ln(\eta^*/a))$ are placed on oblique lines similar to the ones in Fig. 6c but only one point per line is recorded. These lines move upwards and downwards and with a sufficiently large amount of data, the points finally fill a parallelogram.

The two horizontal sides of the parallelogram correspond to the minimum and maximum measured amplitude, η_{min} and a, respectively where η_{min} is the threshold of the measurement technique. The lower and upper oblique lines are related to $\eta_0 = \eta_{0,min}$ and $\eta_0 = \eta_{0,max}$, i.e. the minimum and maximum values of the initial magnitude of perturbation (see the paragraph on the initial disturbance level below). The mean spatial growth rate is determined from the centre line of the parallelogram (see Fig. 10). The mean spatial growth rate k_i is measured from the slope of the mean line on sets of 500 to 5000 points.

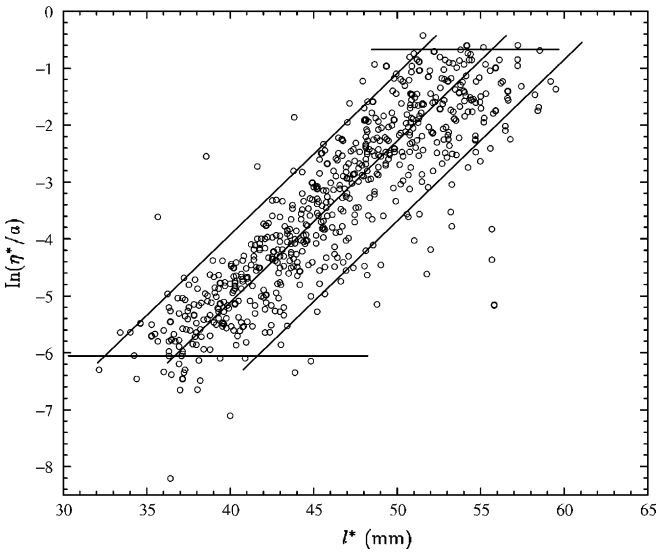

Fig. 10. *Statistical diagram*. $\ln(\eta^*/a) = f(l^*)$. Experimental points fill a parallelogram. The mean slope of the linear regression represented by the continuous line is used to compute the mean growth rate of perturbations ($L/2a = 27$, $U_l = 1.70$ m/s).

An attempt to use a mean image to determine the mean position of the wave crests failed. In fact, the swells and the necks are lost in the mean image as there is no phase relation in a series of images. At a given downstream position, the probability density function of the interface radial position is centred on the centre of oscillations, i.e. on the extrapolated undisturbed interface position, and the growth rate cannot be determined.

The variation of the non-dimensional spatial growth rate $\tilde{k}_i = ak_i$ with the liquid jet velocity is compared to the linear analysis in Fig. 11. The points are plotted for $|\tilde{k}_i|$ versus U_f, as growth rates are effectively measured near the end of the jet, so at a downstream position where the jet is accelerated. U_f is taken from the measurement of c for the nozzles $L/2a = 10$, 27 and 200. For the nozzle $L/2a = 125$ it is supposed that the limit $U_f = (4/3)U_l$ is reached as soon as in the case of $L/2a = 200$. In all the cases the spatial growth rate is non-dimensionalised by the final jet radius a_f derived from Eq. (19).

For the Rayleigh regime ($U_l < U_c$), the spatial growth rate decreases as predicted by the theory. At the critical point the growth rate starts to deviate from the theory and increases rapidly, whereas it continues to decrease in the theory. The critical velocity of IFBM regime jets is then related to a change of the growth rate and not only to a change of the initial disturbance level as proposed by Phinney (1972) and others. The theory must be improved to predict this increase. Sterling and Sleicher (1975) introduced a modification of their dispersion equation to better fit the experimental critical velocity. They introduced a correction coefficient C_s for the inertial term (ρU^2). An artificial attenuation or amplification of the inertial term on the jet stability is obtained whether C_s is lower or greater than one respectively. Sterling and Sleicher and also Leroux et al. (1996) fitted the modified theory to their breakup length measurements by an appropriate choice of C_s. An attempt to use this modified theory failed. A value of C_s greater than one was used in

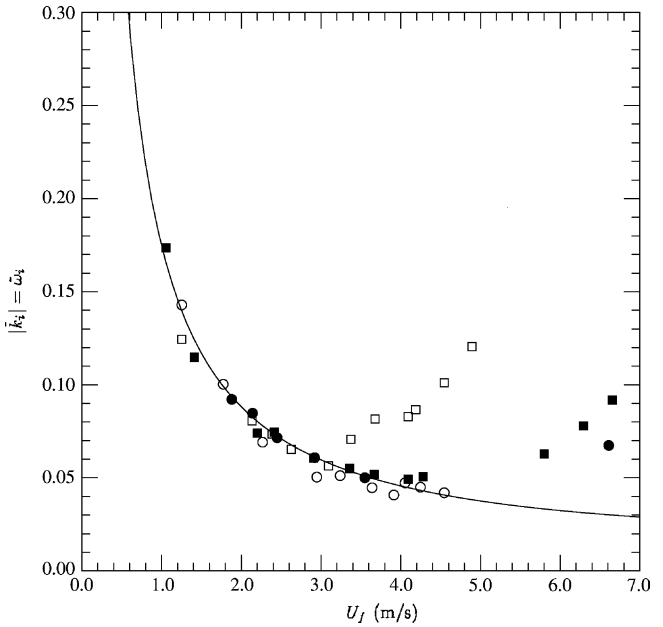

Fig. 11. *Non-dimensional growth rate.* (●), $L/2a = 10$; (○), 27; (■), 125; (□), 200. The non-dimensional growth rate is derived from statistical measurement of k_i and from the final jet radius a_f given by Eq. (19) $|\tilde{k}_i| = |k_i|a_f = \tilde{\omega}_i$. Experiment and linear theory (continuous line) are in good agreement up to the critical point for each nozzle.

our case to lower the critical point of the theoretical curve. The consequence is a global increase of the growth rate for all the values of U_l, so the entire curve for $|k_i(U_l)|$ is modified and not only the part for $U_l > U_c$. The prediction of the modified theory then deviates from the experiment even for the Rayleigh regime, so it is not satisfactory. The steep increase for $U_l > U_c$ cannot be predicted in this way and a deeper modification of the theory should be considered.

The steep change is particularly evident from the plot of dimensional ω_i versus U_l/U_c in Fig. 12. Results derived from Rayleigh and Weber theories are also reported in this figure. As the jet velocity is normalised by U_c, the different curves for the modified and non-modified theory of Weber ($C_s \neq 1$ or $C_s = 1$) are superimposed. Two distinct trends are clearly shown on this plot. For $U_l \leqslant U_c$ the dimensional rate of growth remains constant as in the Rayleigh theory. A steep increase occurs for $U_l > U_c$. The steep increase of the growth rate at $U_l/U_c \simeq 1$ results from the crossing of a threshold for some characteristics of the jet flow. This threshold is not related to the action of the ambient air, as the critical velocity does not depend on the ambient air pressure for these jets, but to the internal flow as said before. Rupe (1962) suggested that the decay of a fully developed laminar profile leads to the creation of a radial pressure gradient responsible for the appearance of a radial velocity component in the flow. From a simple energy budget, Harmon (1955) showed that one ninth of the total kinetic energy is lost during the relaxation process when the initial profile is parabolic. This energy change is large compared to what might be expected to go into the formation of the jet surface, and Harmon concluded that a majority of the loss must be due to viscous dissipation. In the case of water jets, the viscous dissipation should be weak as the viscosity is small. A part of the lost energy may contribute to the appearance of perturbations in

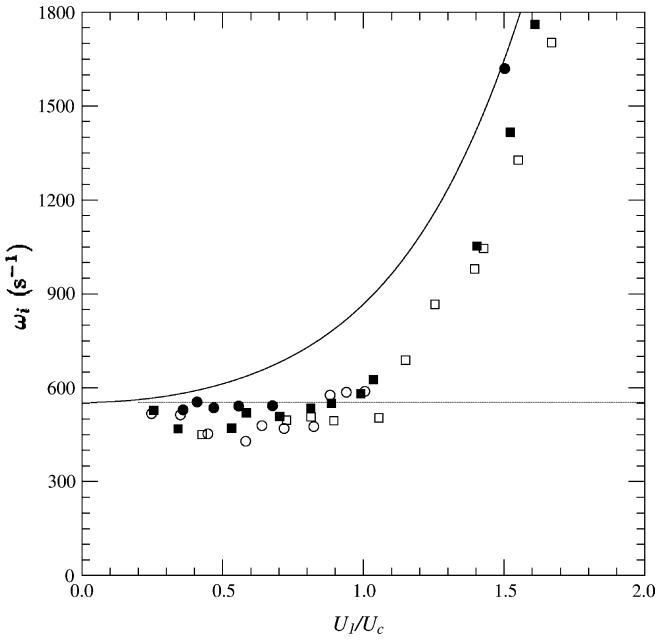

Fig. 12. *Dimensional temporal growth rate.* (●), $L/2a = 10$; (○), 27; (■), 125; (□), 200. Dashed line and continuous line are respectively for Rayleigh and Weber theories. Modified and non-modified Weber theories ($C_s \neq 1$ and $C_s = 1$) are superimposed in the plot versus velocity ratio U_l/U_c as the modification results in the modification of the critical velocity only. The growth rate ω_i remains constant for $U_l \leqslant U_c$ and then increases rapidly. The linear theories are not able to predict such a sudden increase.

the form of a radial velocity component. The amount of energy redistributed during the relaxation phenomenon depends on the rate of change of the velocity profile along the jet axis and also on the total amount of energy crossing the nozzle outlet. This latest quantity is strongly related to the velocity profile at the exit. The kinetic energy passing through the nozzle outlet per unit time, $\dot{K}_{E0}$, is proportional to U_l^3 times a coefficient α function of the velocity profile. When changing from a parabolic to a flat profile, Harmon (1955) showed that α is divided by two. So for a long tube from which the velocity profile at the outlet remains parabolic, a very low mean velocity implies a low value for $\dot{K}_{E0}$, but when U_l increases, $\dot{K}_{E0}$ increases faster due to the cubic dependency. As the profile remains parabolic, α remains maximum and the energy potentially available for a modification of the jet stability increases rapidly. The energy threshold above which the instability process changes could be reached for a low mean velocity in this case. When the nozzle length decreases, α decreases and thus $\dot{K}_{E0}$. The relaxation phenomenon is also less significant, so the amount of energy transferable to the instability of the jet through the profile relaxation phenomenon is lowered. The threshold is reached at a higher mean velocity. For the limit case of a flat profile at the nozzle exit, there is no relaxation effect and thus no energy transfer is possible from the mean flow to the instability. No threshold exists in this case and the jet behaves as predicted by the Weber theory.

The critical velocity of IFBM regime jets characterises the threshold above which the instability process changes. The decrease of U_c with the increase of the nozzle length is consistent with the

energy redistribution scheme presented above. It was verified that the loss of kinetic energy $\dot{K}_{E0} - \dot{K}_{Ef}$ increases with U_l (where the final kinetic energy $\dot{K}_{Ef} = \pi\rho_l a^2 U_l c^2/2$). However, only a part of $\dot{K}_{E0} - \dot{K}_{Ef}$ is supposed to go into the destabilisation of the jet, the other part being dissipated by viscous effects. The value of the energy threshold related to the critical point could be evaluated if this quantity was known, but a better knowledge of the liquid flow characteristics and particularly the way the velocity profile evolves along the jet axis is needed.

Penchev and Radev (1977) studied in a numerical approach the effect of the velocity rearrangement on the stability of a contracting jet in a liquid–liquid system. They found that the critical point can be shifted towards a greater velocity when the profile relaxation is taken into account. Radev et al. (1983) studied the stability of a capillary jet surrounded by an immiscible liquid but gave in addition an example of application of their numerical approach for the case of a water jet flowing into the air. Contrarily to Leib and Goldstein (1986a) or Ibrahim and Marshall (2000), they found that the parabolic profile is more unstable than the uniform profile and that the maximum growth rate decreases along the jet axis when considering an initial parabolic velocity profile. However, no indication is given on the effect of the variation of U_l on the jet stability for a water jet surrounded by air. For the case of a liquid–liquid system (carbon tetrachloride jet flowing into water), Radev et al. found that the growth rate and the wave number increase along the jet axis, so when the velocity profile progressively relaxes. They explain that this trend, which is quite the opposite of what they obtained when the liquid jet is surrounded by a gas, is due to the weaker decrease of the velocity profile gradient in the liquid–liquid system as a result of the strong interaction between the jet and the medium. The main difference between the analysis of Radev et al. and those of Leib and Goldstein or Ibrahim and Marshall lies in the consideration of the viscous effects in the former whereas Leib and Goldstein and Ibrahim and Marshall considered only the response of the jet to the velocity profile. In other words, the whole jet is supposed to be under the influence of a given velocity profile in the analyses of Leib and Goldstein and Ibrahim and Marshall whereas Radev et al. considered the rearrangement of this profile under the action of the shear stress due to the viscosity of the fluids.

It is evident from the works cited above that the velocity profile and the change of this profile along the jet acts on the jet stability. However, none of these works mentioned a possible steep increase in the variation of the growth rate versus liquid jet velocity as observed for IFBM regime jets.

3.4. Initial disturbance level

To determine the initial disturbance level η_0 it is supposed that the growth rate remains constant along the jet. This hypothesis can be considered as questionable, since the growth rate should change with the velocity profile and the velocity profile evolves along the jet axis. The determination of η_0 is also subject to uncertainty due to the distance of the measurement points (near $z = L_{bu}$) from the nozzle exit ($z = 0$). The experimental values for η_0 must, therefore, be considered with the greatest care.

The initial disturbance level is evaluated for each wave in the time-resolved diagrams $\ln(\eta_m/a) = f(z_m)$ from the crossing of the wave lines with the vertical axis at $z_m = 0$. It was found that η_0 is not distributed randomly but oscillates in time. The perturbations are marked by the order of appearance on the jet in Fig. 6c. Among the six waves, the wave number 1 presents the

lowest amplitude at every downstream position. From waves 1–5 there is an increase of the amplitude, i.e. the lines are shifted upwards in the diagram. Then, for waves 6 and after, the lines are arranged downwards (the waves after the 6th are not presented here to keep the diagram plot clear). When the lower line is reached again, the following wave lines move upwards to the upper position and then downwards and so on. The value of η_0, obtained by extrapolating the diagram up to the nozzle exit, oscillates in time as the waves are triggered at the nozzle exit. For the example of Fig. 6, an oscillation frequency $\simeq$65 Hz is measured whereas the pulsation frequency of the disturbances $f = 650$ Hz is consistent with the theory of Rayleigh ($\simeq$630 Hz). A low frequency phenomenon seems to act on the jet. This particular feature of jet stability has not been reported in previous experimental studies, to our knowledge. Such a low frequency mode can be compared to the results of Keller et al. (1973) who found that some unstable modes, which grow much more rapidly than the others, have very long wavelengths and, as a result of the short length of the jet, are not observed in experiments. For the flow condition of the example of Fig. 6 and with a pulsation of 65 Hz, the wavelength of such a mode, given by Eq. (13) in Keller et al. (1973), is two times larger than the breakup length of the jet. This disturbance wavelength can effectively not be measured on the jet. The reason why such perturbation modes are observed in the present study is surely related to the use of a time-resolved apparatus.

The initial amplitude η_0 is typically bounded between 10^{-3} and 1 nm corresponding respectively to $\ln(\eta_0/a) = -19.5$ and $\ln(\eta_0/a) = -12.6$. This latest value is comparable to the results of Grant and Middleman (1966) ($\ln(\eta_0/a) \simeq -13.4$) or Weber (1931) ($\ln(\eta_0/a) = -12$). The minimum reached by η_0 seems extremely small when compared to inter-molecular length in water $l_{\mathrm{im}} \simeq$ 0.3 nm, and not physically reliable in terms of interface displacement. It could be expressed in terms of thermodynamic variable fluctuations, like temperature or pressure, but a different explanation is proposed here. Leib and Goldstein (1986a) studied the response of a liquid jet to imposed disturbances under velocity distribution ranging from the plug flow profile to the fully developed laminar flow profile. They showed that the plug flow profile is much more unstable than the parabolic profile in terms of both growth rates and range of unstable frequencies. For the fully developed profile they claimed that there is virtually no growth for realistic values of the flow parameters, but the neutral disturbances can ultimately turn into amplifying waves as the profile relaxes toward a plug flow. Ibrahim and Marshall (2000) have also demonstrated that under parabolic condition, the jet remains stable. They used the same family of velocity profile as Leib and Goldstein, $U(r) = (1 - br^2)/(1 - b/2)$, where the parameter b goes from 0 for plug flow to 1 for parabolic profiles. Ibrahim and Marshall explored both Rayleigh and atomization regimes and showed that for $We < 500$, the critical value b_{cr} of the parameter b, above which the jet is stable, decreases with We. So for the Rayleigh regime, the range of profiles leading to unstable conditions is reduced when U_{l} increases. For the range of Weber numbers covered in the present study ($We < 200$), this indicates that only quasi-flat profile conditions lead to unstable jets, and perturbations on liquid jets with a non-flat profile remain neutral up to a downstream position where the profile has relaxed. So there must be a neutral region at the start of the liquid jet along which the perturbations do not grow.

The region of neutral disturbances has not been explored in the present experiment due to the low sensitivity of the experimental technique that prevents measurement of disturbance levels under 3 μm. The initial disturbance level is only determined by extrapolating the measurements up to the nozzle exit but the presence of a neutral region at the nozzle exit induces a shift of the

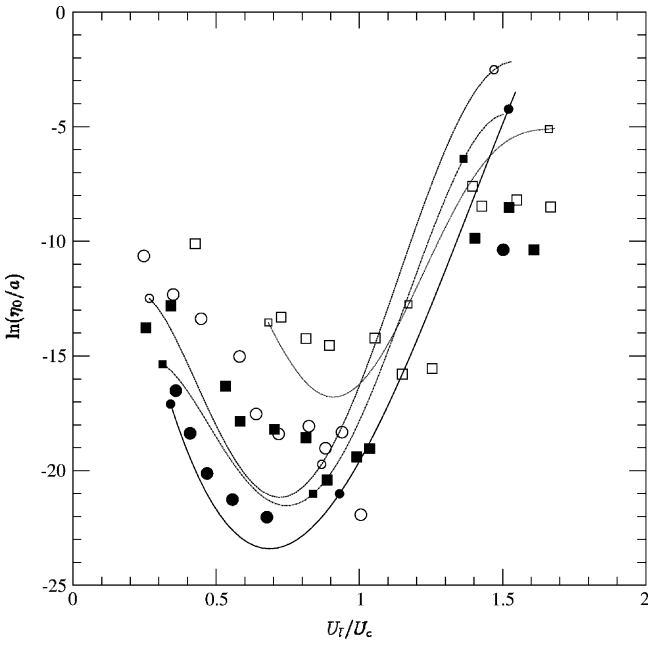

Fig. 13. *Initial disturbance level.* (●), $L/2a = 10$; (○), 27; (■), 125; (□), 200. Initial disturbance levels do not remain constant in the Rayleigh regime ($U_l < U_c$) contrary to what is commonly supposed, but decrease as far as $U_l/U_c \simeq 1.3$. The very low values reached by η_0 are explained by the appearance of a neutral region at the nozzle exit. The length of this region increases up to the critical point. The jump in the values of η_0 corresponding to the removal of the neutral region happens at the critical point or just after the critical point. Continuous lines correspond to the computation of $\ln(\eta_0/a)$ with Eq. (21). The minimum is slightly shifted before the critical point but the same trend is obtained.

diagram points towards downstream positions. The lowest values of η_0 can be related to a neutral region length $L_{nr} \simeq 30$ mm.

The mean initial magnitude of perturbation is given by the ordinate at $z = 0$ of the linear regression line in the diagram $\ln(\eta^*/a) = f(l^*)$. It has been shown that η_0 can be taken as an indicator of the length of the neutral region where the perturbations remain stable. The variations of $\ln(\eta_0/a)$ with U_l/U_c are plotted in Fig. 13 and compared to the values obtained from Eq. (21) derived from Weber's theory

$$\ln\left(\frac{\eta_0}{a}\right) = -\frac{1}{\sqrt{We}(1+3Oh)}\frac{L_{bu}}{2a} \tag{21}$$

where $Oh = \mu/\sqrt{2a\rho_l\sigma}$ is the Ohnesorge number. The initial disturbance level decreases with U_l in the Rayleigh regime down to the critical point, and then a steep increase occurs. The same trend is given by Eq. (21). In terms of neutral region lengths, these results indicate that there is an initial increase of L_{nr} up to the critical point where $L_{nr}/a \simeq 100$. The increase of the neutral region length with U_l is consistent with the results of Ibrahim and Marshall (2000) who found that the range of profiles leading to unstable conditions reduces when U_l increases. So the portion of the jet concerned with neutral disturbances increases with U_l. The steep increase of η_0 indicates that there is no longer any neutral region for $U_l > U_c$.

Phinney (1972) found from the application of Eq. (21) that the initial disturbance level follows a plateau in the first part of its variation with U_l, even though he considered only data for which the influence of the ambient air was negligible, as in the present case. The difference comes from a difference in the viscous time scales. In the present experiment the value of the Ohnesorge number ($Oh = 6.3 \times 10^{-3}$) corresponds to the lowest values in the analysis of Phinney whereas Reynolds numbers are of the same order of magnitude. The viscous time over capillary time ratio is thus higher in our experiment, indicating that the relaxation process takes longer. This can explain that a neutral region actually exists and is detectable in our experiment. Moreover, in Fig. 1 of Phinney (1972), the points for the lowest values of Oh ($Oh = 4.34 \times 10^{-3}$ and 6.14×10^{-3}) show the same trend, namely $\ln(\eta_0/a)$ initially decreases before increasing when passing the critical point. So for low viscous jets, the relaxation of non-flat profiles at the nozzle exit induces a neutral region with a length of the same order of magnitude as the breakup length. This neutral region is only present in the Rayleigh regime and disappears when the critical point is passed.

3.5. Wave number

The wave number also presents a sudden increase around the critical velocity (see Fig. 14a). Two domains are clearly identified in Fig. 14a, corresponding to $k_r \simeq 0.7$ in the Rayleigh regime, and a sharp continuous increase of k_r located near $U_l/U_c \simeq 1.25$ up to $k_r \simeq 1.75$. The steep increase of k_r supports the hypothesis of the crossing of a threshold in the breakup process of such jets and confirms that the stability of these jets is totally different from that of ABM regime jets. Weber's theory predicts a gradual increase of k_r shown by the continuous line in Fig. 14a. The

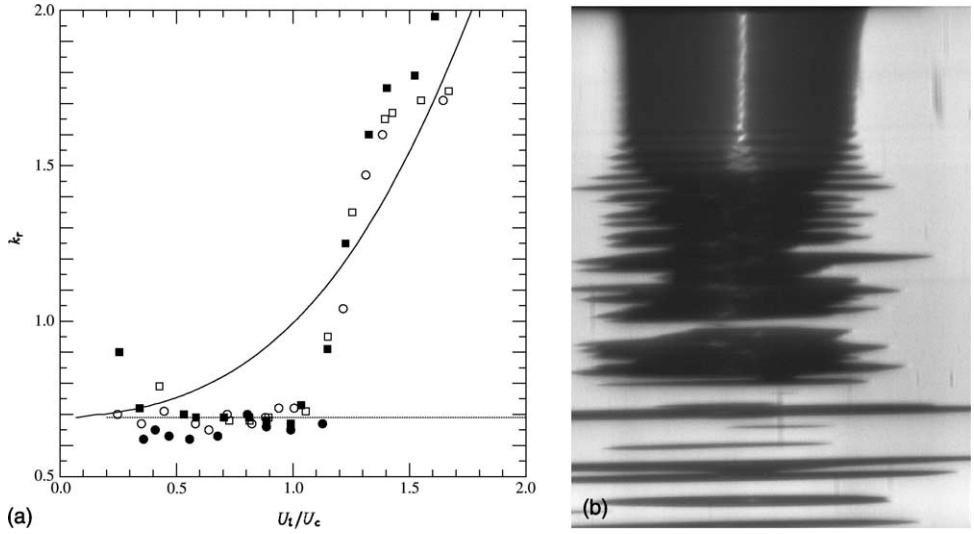

Fig. 14. (a) *Non-dimensional wave number.* (●), $L/2a = 10$; (○), 27; (■), 125; (□), 200. Dashed line and continuous line are respectively for Rayleigh and Weber theories. (b) *Jet shape.* When $U_l/U_c > 1$, the small wavelength initial disturbances grow linearly but do not lead to the breakup of the jet. Surface tension forces the jet to change its shape. Final disturbances have a wavelength of the order of the one given by the theory of Rayleigh. The jet finally breaks into drops of diameter of the same order of magnitude than before the critical point.

good superimposition of the points in the increasing portion of k_r versus U_l/U_c indicates that the steep change occurring around the critical point is not an artifact but the manifestation of an underlying phenomenon. The value reached by the wave number is around 2.5 times the value for the Rayleigh regime. The cutoff wave number $k_{cutoff} = 1$ is then over-stepped when $U_l > U_c$. For such values of k_r the perturbations are usually considered to be stable and high wave numbers are generally reached in ABM regime jets for liquid jet velocity 3–4 times higher (i.e. for $U_l \simeq 20$ m/s).

An increase of the wave number induces a decrease of the droplet diameter. In the limit case of atomization, the droplet diameter is actually much smaller than the jet diameter. The droplets produced by IFBM regime jets should be smaller than those produced by jets in the Rayleigh regime. Malot and Dumouchel (2001a) showed, however, that it was not the case. They found a similar mean diameter size when the jet regime changed from Rayleigh mode to IFBM. Only the size distribution changes and becomes larger. In fact, the initially growing waves of small wavelength do not lead to the breakup of IFBM regime jets. This was verified for jets with $U_l > U_c$ like the one presented in Fig. 14b. The growing disturbances have a very small wavelength (upper hand side of the image). For these small wavelengths, the surface tension has a stabilizing effect, so, after a region of wave growth, a non-growing region covering 5–10 wavelengths appears. This region of constant wave amplitude is the link between the initial growing waves and the final breaking disturbances. Indeed, the 'naturally' unstable large wavelength waves (Rayleigh) dominate the small wavelength waves and the jet finally breaks into droplets of larger diameter than would have been produced by the initial disturbances. The self-driven rearrangement of the wavelength that occurs for IFBM regime jets implies that the range of wavelength of the naturally occurring waves is quite large. This leads to a spreading of the droplet size distribution as observed by Malot and Dumouchel (2001a).

4. Conclusion

The stability of jets controlled by internal flow properties has been studied. Wavelengths, magnitude and growth rates of natural perturbations were measured on the contour of the jets, in addition to the breakup length. Attention was focused on the variation of the quantities close to the critical point. Time-resolved measurements have made it possible to control the linear increase of $\ln \eta$ with time and space and also to observe an oscillatory behaviour of the initial disturbance level.

Jets in the Rayleigh regime present a neutral region at the nozzle outlet along which the perturbation waves remain stable. This neutral region was deduced from initial disturbance level values and it seems that this region only occurs for very low Ohnesorge number jets. It was found that this neutral region is correlated to the part of the jet concerned with the relaxation of the velocity profile. In fact, this relaxation takes a long time when viscous forces are weak, i.e. when Oh is low. The neutral region length increases with U_l and makes the jets longer than they would be with immediately increasing perturbation waves. As soon as the critical point is passed, there is no longer any neutral region. The critical point marks a threshold in the destabilization process which leads the liquid jets to change from the Rayleigh mode regime to the IFBM regime. The growth rate as well as the wave number steeply increase with the liquid jet velocity after the critical point. These steep increases have never been observed from breakup length measurement experiments, nor can they be related to any theoretical analysis available. The increase of the wave

number, however, does not lead to the production of small size droplets, as a wavelength rearrangement occurs before the breakup.

A scheme based on a kinetic energy balance was proposed to correlate the variation of the critical velocity with the nozzle length to the velocity profile relaxation. Part of the kinetic energy passing through the nozzle exit is lost during the relaxation process. It is supposed that not all this lost energy goes into the production of the liquid jet surface. Part of it goes into viscous dissipation, but as has been said before, viscous effects are relatively weak in water, so dissipation should not be the only phenomenon involved. The mechanical energy redistribution can contribute to the instability in the form of a radial velocity component. If the energy injected into the radial velocity component exceeds a certain threshold, then the destabilization mode of the liquid jet changes. The existence of a threshold in the destabilization process corresponds to the development of sub-critical instabilities, as already mentioned by Malot and Dumouchel (2001b). The energy redistribution scheme is in qualitative agreement with experimental observations. The energy available is greater for the long tubes (when the velocity profile is parabolic or nearly parabolic at the nozzle exit) so the threshold (the critical point) is reached at lower jet velocity in this case. A more complete description of the flow characteristics is needed however for a quantitative approach to be considered. The objectives for future works should be the determination of all the relevant controlling parameters acting on IFBM regime jets and the quantification of these parameters at the transition between Rayleigh and IFBM regimes.

The appearance of an initial neutral region in the disturbance of the liquid jet or the change from the Rayleigh mode regime to the IFBM regime are explained through the effect of the relaxation of the velocity profile. However, velocity profiles were not directly measured. Only CFD computations were carried out to access the velocity profile at the nozzle exit. Experimental techniques are lacking for this purpose. The development of velocity measurement techniques applicable in the case of jet flows of very small diameter must remain one of the main objectives, in furthering our understanding of liquid jet breakup phenomenon.

The change of the liquid jet stability characteristics with the velocity profile has also been used to deduce the occurrence of the neutral region. The sensitivity of the measurement technique used in the present study is too low to measure the very low disturbance levels that would be measured in the first part of the jet. The determination of perturbation wave amplitudes over the entire length of the jet represents a challenge for future work on jet stability. This could be achieved by the juxtaposition of different techniques along the jet, each one corresponding to a certain range of disturbance levels.

References

Blaisot, J.-B., Adeline, S., 2000. Determination of the growth rate of instability of low velocity free falling jets. Exp. Fluids 29, 247–256.

Bogy, D.B., 1979. Drop formation in a circular liquid jet. Annu. Rev. Fluid Mech. 11, 207–228.

Collicott, S.H., Zhang, S., Schneider, S.P., 1994. Quantitative liquid jet instability measurement system using asymmetric magnification and digital image processing. Exp. Fluids 16, 345–348.

Eggers, J., 1997. Nonlinear dynamics and breakup of free-surface flows. Rev. Mod. Phys. 69, 865–928.

Goedde, E.F., Yuen, M.C., 1970. Experiments on liquid jet instability. J. Fluid Mech. 40, 495–511.

Grant, R.P., Middleman, S., 1966. Newtonian jet stability. AIChE J. 12, 669–678.

Harmon, D.B., 1955. Drop sizes from low speed jets. J. Franklin Inst. 259, 519–522.
Ibrahim, E.A., Marshall, S.O., 2000. Instability of a liquid jet of parabolic velocity profile. Chem. Eng. J. 76, 17–21.
Iciek, J., 1982. The hydrodynamics of a free, liquid jet and their influence on direct contact heat transfer-I. Hydrodynamics of a free, cylindrical liquid jet. Int. J. Multiphase Flow 8, 239–249.
Karasawa, T., Masaki, T., Abe, K., Shiga, S., Kurabayashi, T., 1992. Effect of nozzle configuration on the atomization of a steady spray. Atomization Sprays 2, 411–426.
Keller, J.B., Rubinow, S.I., Tu, Y.O., 1973. Spatial instability of a jet. Phys. Fluids 16, 2052–2055.
Leib, S.J., Goldstein, M.L., 1986a. The generation of capillary instabilities on a liquid jet. J. Fluid Mech. 168, 479–500.
Leib, S.J., Goldstein, M.L., 1986b. Convective and absolute instabilities of a viscous liquid jet. Phys. Fluids 29, 952–954.
Leroux, S., Dumouchel, C., Ledoux, M., 1996. The stability curve of Newtonian liquid jets. Atomization Sprays 6, 623–647.
Leroux, S., Dumouchel, C., Ledoux, M., 1997. The breakup length of laminar cylindrical liquid jets. modification of Weber's theory. In: ICLASS-97, Seoul, Korea, pp. 353–360.
Lin, S.P., Lian, Z.W., 1990. Mechanisms of the breakup of liquid jets. AIAA J. 28, 120–126.
Lin, S.P., Reitz, R.D., 1998. Drop and spray formation from a liquid jet. Annu. Rev. Fluid Mech. 30, 85–105.
Malot, H., Dumouchel, C., 2001a. Analysis of the drop size distribution of sprays produced by plain cylindrical jets: Application of the maximum entropy formalism. In: ILASS-Europe 2001, Zurich.
Malot, H., Dumouchel, C., 2001b. Experimental investigation of the drop size distribution of sprays produced by low-velocity Newtonian cylindrical liquid jet. Atomization Sprays 11, 227–254.
McCarthy, M.J., Molloy, N.A., 1974. Review of stability of liquid jets and the influence of nozzle design. Chem. Eng. J. 7, 1–20.
Penchev, I.P., Radev, S.P., 1977. Analysis of the stability of a contracting jet in a liquid–liquid system. Theor. Appl. Mech. 8, 16–22.
Phinney, R.E., 1972. Stability of a laminar viscous jet—the influence of the initial disturbance level. AIChE J. 18, 432–434.
Radev, S., Chavdarov, B., Penchev, I., 1983. On the instability of a liquid capillary jet flowing into an immiscible liquid. Theor. Appl. Mech. 14, 70–78.
Lord Rayleigh, 1878. On the instability of jets. Proc. London Math. Soc. 10, 4–13.
Rupe, J.H., 1962. On the dynamic characteristics of free liquid jets and a partial correlation with orifice geometry. Tech. report 32-207, Jet Propulsion Laboratory, California Institute of Technology, Pasadena, California.
Sterling, M., Sleicher, C.A., 1975. The instability of capillary jets. J. Fluid Mech. 68, 477–495.
Weber, C., 1931. Zum zerfall eines flüssigkeitsstrahles. Zeitschrift fuer Angewandte Mathematik und Mechanik 11, 136–141.
Yarin, A.L., 1993. Free liquid jets and films: hydrodynamics and rheology. Longman, Wiley.